Magnet Losses in Inverter-Fed Two-Pole PM Machines

A. Garcia Gonzalez, J. Millinger and J. Soulard, *Member, IEEE*

***Abstract*—This article deals with the estimation of magnet losses in a permanent-magnet motor inserted in a nut-runner. This type of machine has interesting features such as being two-pole, slot-less and running at a high speed (30000 rpm). Two analytical models were chosen from the literature. A numerical estimation of the losses with 2D Finite Element Method was carried out. A detailed investigation of the effect of simulation settings (e.g., mesh size, time-step, remanence flux density in the magnet, superposition of the losses, etc.) was performed. Finally, calculation of losses with 3D-FEM were also run in order to compare the calculated losses with both analytical and 2D-FEM results. The estimation of the losses focuses on a range of frequencies between 10 and 100 kHz.**

***Index Terms*—Eddy currents, 2D-FEM, 3D-FEM, magnet losses, nut-runner, PM motor, slot-less winding.**

I. Introduction

In general, a nut-runner system is composed by an electrical motor fed by a converter via a filter [1]. New emerging technologies like Silicon Carbide (SiC) transistors, allow a higher switching frequency and in consequence a possible reduction of the size of both inverter and filter [2]. However, it is of prime importance to estimate the consequences of a component change in the performance of the motor, for example in terms of losses. Rare-earth elements used in the manufacturing of the magnets used in PM machines are critical due to the elevated prices they have reached in recent years [3]. Hence, it is appropriate to investigate thoroughly how to best design the magnets in the motor.

Many articles about losses in magnets of PM machines have been published recently. However, there are certainly few articles reporting both 3D-FEM simulations and validations through experimental measurements. Furthermore, only [4] and [5] proposed models of machines with similar characteristics to the machine studied in this project (i.e., slot-less with a magnetized ring). However, the results obtained when implementing the models described in these articles were not satisfactory and in consequence other models were investigated. Since these models neglect the end-effects, it is necessary to investigate to which extent they are adequate for calculating the losses in the machine under study, where the length of the magnet is lower than the magnet width ($l < w$).

The main goal of this article is to enhance the interpretation of the losses appearing in the magnets of a PM machine as a result of the harmonics fed by the Pulse Wide Modulation (PWM) in the inverter. Furthermore, different parameters when calculating magnet losses in FEM software are studied for 2D and 3D models. The main dimensions of the machine and the working characteristics are presented in Section II. In order to predict the value of magnet losses, an extensive literature review was performed. Section III is devoted to the description of the analytical models selected to determine the losses in the magnets. The influence on the losses of mesh elements size, time-step and the remanence flux density of magnet material is studied and presented in Section IV. In addition, the evaluation of the principle of superposition, simulations at zero speed of the rotor and 3D-FEM results are included. The analysis of the results obtained by analytical models, 2D and 3D-FEM simulations is presented in Section V. Lastly, conclusions are drawn and future work is proposed.

II. Description of the Machine

A. Main dimensions

The main dimensions of the slot-less machine analysed in this study are shown in table I. The analytical calculations and 2D and 3D FEM simulations were performed on a machine with a length equal to a single magnet segment l.

TABLE I: Main machine dimensions.

PARAMETER	VALUE
Active length L_a [mm]	65
Maximum speed n_{max} [rpm]	30000
Air-gap length l_g [mm]	0.5
Number of winding turns per phase N_c	65
Magnet axial length l [mm]	4.5
Magnet thickness h [mm]	5
Magnet radius R_m [mm]	7.5
Shaft diameter R_r [mm]	2.5
Inner stator diameter R_s [mm]	23.2
Outer stator diameter [mm]	31
Number of poles p	2
Peak phase current I [A]	1
Fundamental frequency f_0 [Hz]	500
Winding type: distributed $q = 1$	

B. Working characteristics

The machine analysed in this project is applied to the power drive of a nut-runner. The working cycle of this type of machine (figure 1) is divided in two stages. The first, in

A. Garcia Gonzalez is with the Department of Energy Technology, Aalborg University, Aalborg 9220, Denmark (e-mail: agg@et.aau.dk)

J. Millinger is with is with the Department of Electric Power and Energy Systems, KTH Royal Institute of Technology, and with Atlas Copco, Stockholm, Sweden (e-mail: jonasmil@kth.se)

J. Soulard is with is with the Department of Electrical Energy Conversion (E2C), KTH Royal Institute of Technology, SE-10044 Stockholm, Sweden (e-mail: soulard@kth.se)

which the machine is running at maximum speed with zero torque for reaching the tightening point. The second, at which the machine reaches nominal speed as the torque is increased to reach the correct value to be applied to the nut. This study was focused on the first operational stage, since it is this region in which the company manufacturing the nut-runner has more interest.

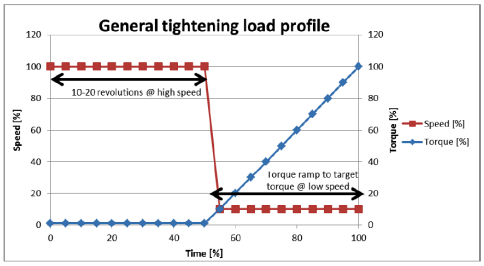

Fig. 1: Typical nut-runner operational characteristic [1].

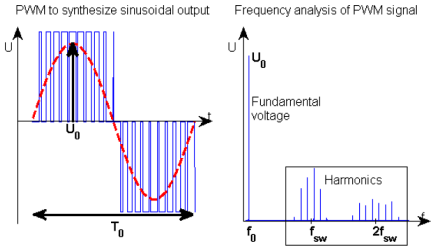

Fig. 2: FFT of PWM voltage [1].

Given the PWM technique implemented in the converter, the running at no-load may involve relatively high losses due to the appearance of harmonics concentrated at 1 time and 2 times the switching frequency f_{sw}. Figure 2 shows the harmonic distribution of the inverter output voltage at no-load. For the coming analyses, it is assumed that the switching frequency f_{sw} is 10 kHz. Additionally, the fundamental frequency f_0 is calculated as $f_0 = n_{max}/60$ where n_{max} is the maximum speed. For this study one harmonic at f_{sw} and one harmonic at $2f_{sw}$ are selected. Thus, the harmonics indexes n_1 and n_2 are given by $n_1 = f_{sw}/f_0$ and $n_2 = 2f_{sw}/f_0$. The harmonic currents applied in the simulations are expressed as:

$$\begin{aligned} I_a &= I\cos(n_1\omega t) + I\cos(n_2\omega t) \\ I_b &= I\cos(n_1(\omega t - 2\pi/3)) + I\cos(n_2(\omega t - 2\pi/3)) \\ I_c &= I\cos(n_1(\omega t - 4\pi/3)) + I\cos(n_2(\omega t - 4\pi/3)) \end{aligned} \quad (1)$$

III. Review of Analytical Models

A. Eddy Currents

The mechanisms governing the eddy currents in a magnet are the same as for the eddy currents in electrical sheets and solid conductors. A time varying magnetic flux density, in this case generated by the mmf of the currents in the stator windings $B_{\delta w}$, penetrates the surface of the magnet. This incident magnetic flux density originates eddy currents as illustrated in figure 3a. It is appropriate to clarify that eddy currents are originated only by time and space harmonics in the stator mmf. That is, the fundamental in space of the mmf at synchronous frequency is seen by the magnets in the rotor as a DC field, consequently, does not create eddy currents. A method to counteract these losses, similar to the lamination technique implemented in a stator core, is the implementation of circumferential and axial segmentations to the magnets [6], [7], [8], [9].

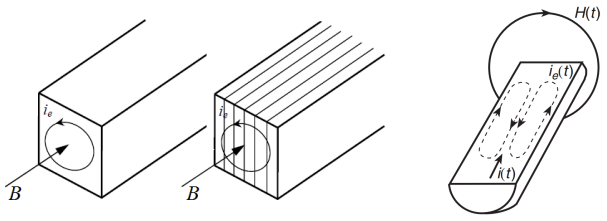

Fig. 3: (a) Eddy currents generation, (b) Skin effect in a long straight round single conductor.

The major consequence of these eddy currents is the heat generated by Joule effect, as the magnets are made of a material with a high conductivity. Additionally, two important phenomena by which the calculation of losses in the magnet can be affected are the reaction field of eddy currents B_{eddy} and the skin effect. The B_{eddy} is generated by the eddy currents themselves, since these are varying in time as well [10]. This B_{eddy} opposes to the external magnetic field $B_{\delta w}$ which is inducing the eddy currents. Consequently, the value of $B_{\delta w}$ is reduced. In addition, $B_{\delta w}$ causes the displacement of the current inside the conductor (figure 3b), being forced to flow close to the conductor's surface. Hence, the effective area is reduced with increasing frequency. This is the definition of skin effect [11].

B. Model neglecting the reaction effect of eddy currents

As described in [12] the calculation of the losses in the magnet when the skin effect is disregarded (low frequencies) is given by the following expression:

$$P_m = \frac{V_m \hat{B}_r^2 \omega_h^2}{16\rho_m} \cdot \frac{w^2 l^2}{l^2 + w^2} \quad (2)$$

Where V_m is the volume of the magnet (assuming that this is of a rectangular section), w is the radial span of the magnet, $\hat{B}_r$ is the peak magnetic flux density in the air-gap due to the mmf of the stator current, ω_h is the electrical angular frequency of the applied harmonic current and ρ_m is the resistivity of the magnet. The assumptions adopted for the calculation of the losses by this model include neglecting skin effect, considering homogeneity of B over the width w of the magnet and neglecting end effects. In addition, this study presents an alternative for the calculation of losses for higher frequencies. Taking [13] as reference, the power losses per area exposed to a field H can be calculated as:

$$P/S = 1/2 \cdot H_{tan}^2 R_s \quad (3)$$

With H_{tan} as the peak tangential incident magnetic field, S being the tangential surface given by $S = 2h(l + w)$, and R_s is the surface impedance $R_s = 1/(\delta_m \sigma_m)$ where δ_m, the skin depth, is given by:

$$\delta_m = \sqrt{\frac{2}{\omega_h \sigma_m \mu_m \mu_0}} \tag{4}$$

With σ_m and μ_m as the conductivity and permeability of the magnet. The criterion for selecting either of the two methods is based on how large the skin depth is in comparison to the magnet dimensions w, h and l. In coming sections of this article these two models are denominated *Huang_a* and *Huang_b*, respectively.

C. Model accounting for the reaction effect of the eddy currents

This model presented in [14] defines the losses in the magnet region as:

$$\begin{aligned} P_{III} = 2\alpha_p \pi L_a R_s^2 \omega_r \mu_0 \mu_m \mu_{sl}^2 \sum_{n=1}^{\infty} \sum_{m=-\infty}^{\infty} \frac{(n+m)}{m} J_{nm}^2 \\ \cdot \mathrm{Re}\left\{ j \frac{C_9}{K} \left[\left(\frac{\tau_m R_r}{m} \mathbf{Y}_{m-1}(\tau_m R_r) - \mathbf{Y}_m(\tau_m R_r) \right) \mathbf{J}_m(\tau_m R_m) \right. \right. \\ \left. - \left(\frac{\tau_m R_r}{m} \mathbf{J}_{m-1}(\tau_m R_r) - \mathbf{J}_m(\tau_m R_r) \right) \mathbf{Y}_m(\tau_m R_m) \right] \\ \cdot \frac{C_9^*}{K^*} \left[\left(\frac{\tau_m R_r}{m} \mathbf{Y}_{m-1}(\tau_m R_r) - \mathbf{Y}_m(\tau_m R_r) \right) \right. \\ \cdot \left(\frac{\tau_m R_m}{m} \mathbf{J}_{m-1}(\tau_m R_m) - \mathbf{J}_m(\tau_m R_m) \right) \\ - \left(\frac{\tau_m R_r}{m} \mathbf{J}_{m-1}(\tau_m R_r) - \mathbf{J}_m(\tau_m R_r) \right) \\ \left. \left. \cdot \left(\frac{\tau_m R_m}{m} \mathbf{Y}_{m-1}(\tau_m R_m) - \mathbf{Y}_m(\tau_m R_m) \right) \right]^* \right\} \end{aligned} \tag{5}$$

Where, the sub-indexes m and n correspond to space and time harmonics, respectively. α_p and ω_r are the pole arc to pole pitch ratio and the rotor angular velocity, respectively. The functions $\mathbf{J}_m$ and $\mathbf{Y}_m$ are Bessel functions of first and second kind of m order, respectively. And the harmonic amplitude of the equivalent current sheet distribution:

$$J_{nm} = \frac{3 N_c I K_{dp\nu} K_{so\nu}}{\pi R_s} \tag{6}$$

Where, $K_{so\nu}$ and $K_{dp\nu}$ the slot opening and winding factors defined in [15]. Other parameters such as C_9, K, τ_m, τ_{sl} and μ_{sl} are described and derived in the reference, as well as, the main assumptions adopted for this model. Therefore, for sake of simplicity and to prevent any misinterpretation, their descriptions are omitted in this article. In coming sections of this document, this model is referred to as *Zhu*.

The analytical models selected were developed for machines with different geometry and characteristics than the slot-less machine under investigation. Therefore, it was required to adapt the expressions to the actual machine. Note that for evaluating the losses with models *Huang_a* and *b*, the magnet ring is assumed to have a rectangular section with a total width of $(R_r + R_m)/2$. On the other hand, for model *Zhu*, the coefficient $K_{so\nu}$ is assumed to be equal to 1, due to the absence of slots in the actual machine. Additionally, the thickness of the retaining sleeve described in the reference is set to zero and the corresponding permeability and conductivity set to 1 and zero, respectively.

IV. FEM Simulations

A. 2D-FEM Simulations

The FEM software selected was FLUX™ v12 from Cedrat. All simulations were performed in the *Transient Magnetic* module. Figure 4 shows the geometry of the 2D model.

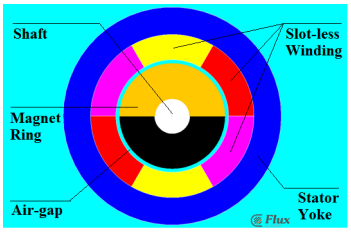

Fig. 4: 2D geometry in FLUX software.

1) Mesh Size Validations: For validating the size mesh required to calculate losses in magnet, three options were adopted. The selection of mesh size was focused on the regions which are believed to be more critical. For all three meshes, the smallest mesh elements are located within the shaft, magnet and air-gap regions. Furthermore, the size of the elements in these regions was selected to be lower than the skin depth of the magnet δ_m at 10 kHz. Additionally, it was decided to link the time-step for each mesh to the size of the elements.

- *Mesh 1: Aided mesh*. For this type of mesh, the aided mesh option was activated. The selection of the time-step in this case, was based on the suggestions from the tutorials of FLUX™. With a number of steps $n_{steps} = 140$ the time-step was selected as $t_{step_1} = T_0/n_{step}$. With T_0 as the period of the fundamental frequency $f_0 = 500$ Hz the time-step was calculated as $t = 14.3\,\mu$s.
- *Mesh 2: Coarse mesh*. This type of mesh is of lower quality when compared with the "aided mesh". Some parameters defining the mesh in the software were set up manually and the aided mesh was disabled. The software offers several options for defining the size of the elements required. Among them, the number of elements that a mesh line should have (*Arithmetic*). A rough calculation of the size of the elements inside the magnet can be done with the perimeter described by the magnet radius R_m and the number of segments n_{seg} defined for this line $size_2 = 2\pi R_m/n_{seg}$. This yields $size_2 = 1.31$ mm which is lower than the skin depth by a factor of 3 approximately. Note that the skin depth for frequencies of 10 and 20 kHz are 5.8 and 4.1 mm respectively (according to equation 4). The definition of the time-step was achieved by introducing $size_2$ in equation 4. An equivalent frequency f_{step2} = 197.11

kHz was obtained. Consequently, the time-step for *Mesh 2* was $t_{step2} = 5.07\,\mu s$.

- *Mesh 3: Fine mesh.* For this mesh type the elements are finer in comparison to those of the "aided mesh". For the calculation of the time-step, similar procedure was followed as for *Mesh 2*. The equivalent frequency for the calculated segment size $size_3$ is f_{step3}= 1404.40 kHz and the time-step $t_{step3} = 0.712\,\mu s$.

The results for each mesh type with its own time-step are shown in figure 5a. The average values of losses for meshes 1, 2 and 3 are; 1.67, 2.67 and 2.81 W, respectively. Showing a highest deviation of 67.95% between *Mesh 3* and *Mesh 1* and the lowest deviation equals to 5.07% between *Mesh 2* and *Mesh 3*.

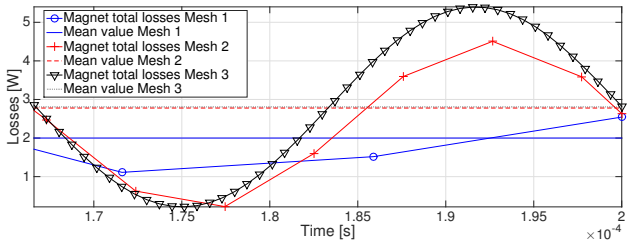

(a)

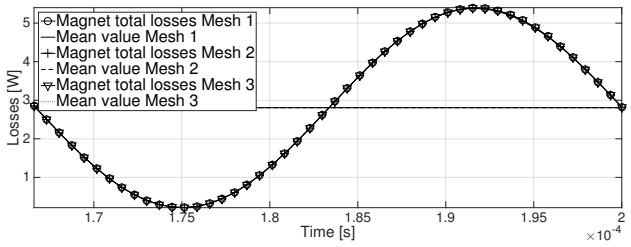

(b)

Fig. 5: Magnet losses for different mesh densities; (a) different time-step, (b) same time-step ($t = 0.712\,\mu s$).

In addition, it was decided to investigate the magnet losses calculated with each mesh type keeping the same time-step (i.e., equals to $t_{step3} = 0.712\,\mu s$). The results are shown in figure 5b. A very good agreement between the three different meshes was obtained with approximately zero deviation. Here an important conclusion may be drawn; the value of the time-step showed to have a stronger effect on the losses than the density of the mesh. In addition, the reduction of both the size of the mesh elements and the value of time-step increased the simulation time. Consequently, it was decided to investigate further the effect of time-step on the calculation of the magnet losses.

2) Time-step validations: As shown in previous sections, the magnet losses were not varying with the size of the mesh elements for the three tested meshes. However, there was a dependence with the time-step, the frequency and the skin depth. Therefore, it was necessary to investigate to what extent the calculation of the losses is affected by changes in the value of the time-step. Thus, the time-step was formulated as a function of the frequency, as $t_{step} = 1/(f_{sw} k_{time})$. Where k_{time} is the number of samples per period. The factor k_{time} was taken from 5 to 50 in steps of 5 and applied to the fine mesh (i.e., *Mesh 3*). The variation of the losses with the number of points per period k_{time} is shown in figure 6. The lower k_{time}, the lower the calculated value of losses and as the number of sampling points increased, the results became more stable converging to a value of 2.64 [W].

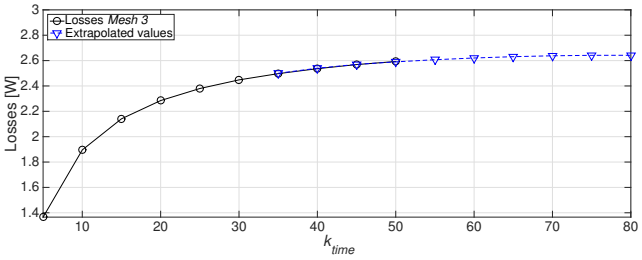

Fig. 6: Magnet losses for different time-step.

The trend is that the deviation in losses between two consecutive values of k_{time} is reducing as the number of samples is increased. Then, it is required to define at which level of deviation is considered that a reliable value has been reached. For example, if it is assumed that the solution is reached when a variation of 1 % is achieved, a number of sampling points $k_{time} = 50$ is required. On the other hand, if a higher level of accuracy is required, the factor k_{time} may increase up to 80. Consequently, the simulation time is increased. Hence, the selection of this factor is a compromise between time and accuracy.

3) Effect of remanence magnetic flux density on losses: These simulations were intended to evaluate the effect that B_r could have in the calculation of the magnet losses. Hence, it was decided to evaluate the losses in two different scenarios:

- *Magnet OFF:* Setting the magnet region as a solid conducting region ($B_r = 0$ T).
- *Magnet ON:* Setting the magnet as a *Linear magnet described by the B_r module*. That is, setting the value of $B_r = 1.12$ T.

In addition to these two scenarios, it was decided to evaluate the effect at a frequency range from 10 to 100 kHz. The losses calculated at 10 kHz are presented in figure 7. The results show a good fit for both cases (magnet ON and OFF). Consequently, the value of the remanence magnetic flux density B_r is not expected to have a significant influence on the losses. Similar results were obtained for a frequency of 100 kHz. In addition, the current density distribution in the magnet is shown in figures 8a and 8b for frequencies 10 and 100 kHz, respectively. Similarly, no influence of B_r in the current density distribution and losses was identified. A symmetrical behaviour of the current density in the magnet was expected. However, an undulating behaviour may be observed in figures 8a and 8b. This is a result of the reaction field of eddy currents B_{eddy}. The skin effect is more pronounced as the frequency increases in figure 8b for a frequency of 100 kHz.

4) Superposition of the losses: It was then verified if the principle of superposition might be applied to the simulations for different harmonic indexes. This was performed keeping

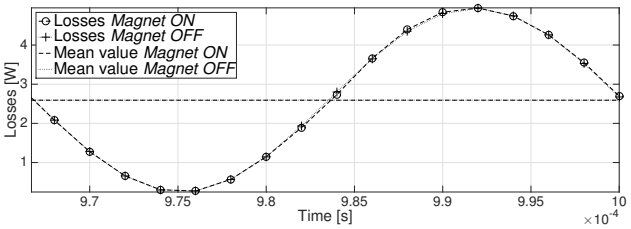

Fig. 7: Magnet losses at 10 kHz magnet on and off.

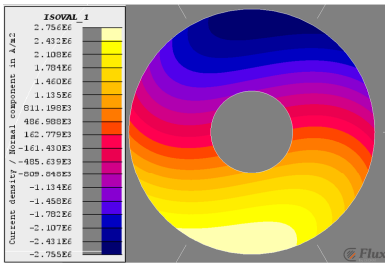

(a)

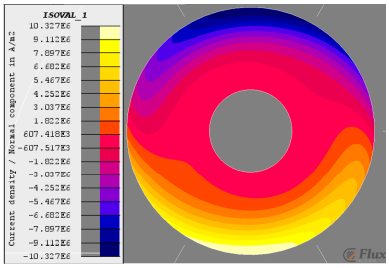

(b)

Fig. 8: Current density distribution magnet off; (a) 10 kHz, $t = 0.5\,\text{ms}$. (b) 100 kHz, $t = 0.1\,\text{ms}$.

the rotor speed at a value of 30000 rpm, and varying the harmonic indexes n_1 and n_2 accordingly in order to obtain a variation of the switching frequency f_{sw} from 10 to 100 kHz in steps of 1 kHz. Three different cases were studied:

- *Case 1*: Losses only due to the harmonic index n_1 and a phase shift of $\pi/3$.
- *Case 2*: Losses only due to the harmonic index n_2 and a phase shift of $\pi/2$.
- *Case 3*: Total losses due to both n_1 and n_2.

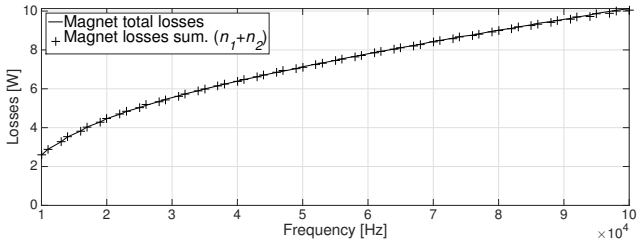

Fig. 9: Magnet losses vs. frequency.

Figure 9 shows that a perfect fit between the two methods was obtained with deviations lower than 1%. This confirms that for this type of machine superposition may be applied and that there will be no interaction between harmonics at f_{sw} and harmonics at $2f_{sw}$.

5) Simulations at zero speed in the rotor: An alternative for running the simulations was setting the speed of the rotor n_{max} as zero. Consequently, the only parameter varying with time would be the applied current. However, it was necessary to determine the direction of rotation of the harmonic indexes n_1 and n_2 in order to define the relative speed of rotation. This condition was evaluated at frequencies of 10 and 100 kHz. Figure 10 shows the results for the losses when the rotor is rotating at a fixed speed and when its speed is set to zero. A similar behaviour was obtained at a frequency of 100 kHz. This machine can be simulated at no speed since the space harmonics from the current loading are negligible. A reduction of the simulation times is expected by using this simulation method. However, in 2D-FEM simulation times were in the same range with both type of simulations.

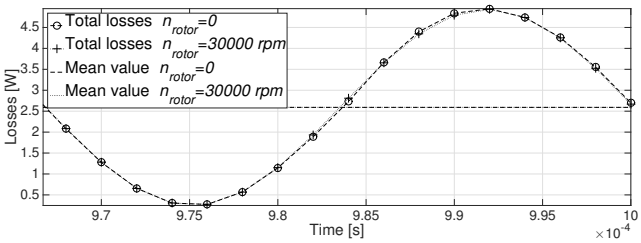

Fig. 10: Losses at 10 kHz.

B. 3D-FEM Simulations

The simulation settings presented in Subsection IV-A apply to the calculation of the losses in 3D-FEM. That is, same time-step factor and a fine mesh were selected in order to guarantee that the values calculated are representative and that a fair comparison can be done with 2D-FEM simulation results. Figure 11a shows the current density distribution over the surface of the magnet at 10 kHz. Yellow colours and large arrows indicate maximum values. At first glance the magnet could be divided into two regions in terms of the eddy current flow indicating the two incident values of $B_{\delta w}$. In addition, some hot-spots of critical regions in which these currents are the highest are identified as the boundaries between the shaft and magnet regions at the top and bottom faces of the magnet. This is due to the curvature described by these regions in which the currents are forced to vary their trajectory.

For performing a better analysis of the behaviour of the eddy currents inside the magnet, a 2D sub-region was defined inside the magnet volume parallel to *xz* axis. The eddy current plots for grid *xz* are shown in figure 11b. As predicted in the literature, the eddy currents are forced to flow in the periphery of the magnet finding a common returning path. The plane *xy* is a transition region in which currents change from the top region to the bottom region, thus closing the loop. The distribution of the losses is shown in figure 12. It follows the behaviour of the eddy currents since the losses are proportional to the square of the current.

The distribution of the losses in the *xy* plane is shown in figure 13. Here it is shown how the distribution of the current density and consequently the distribution of losses has a more symmetrical behaviour. This indicates that B_{eddy}

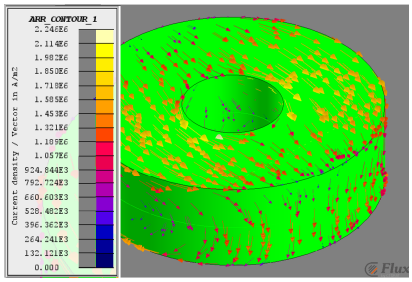

(a)

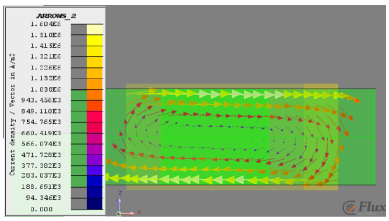

(b)

Fig. 11: Current density distribution at 10 kHz $t = 52\,\mu s$; (a) over the surface, (b) plane *xz*.

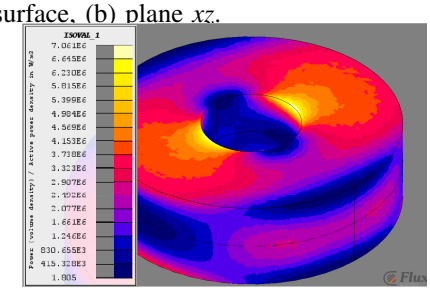

Fig. 12: Magnet loss distribution at 10 kHz; $t = 52\,\mu s$.

in 3D-FEM simulations is less pronounced than for the 2D-FEM simulations.

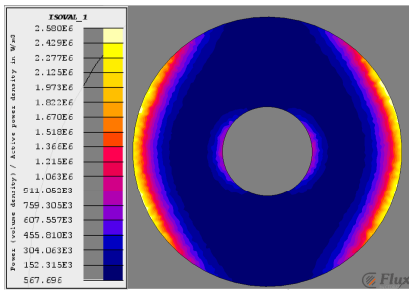

Fig. 13: Magnet loss distribution at 10 kHz; $t = 52\,\mu s$, plane *xy*.

In addition, the superposition principle, the effect of the remanence magnetic flux density of the magnet B_r and simulations of zero speed in the rotor were evaluated for 3D-FEM simulations. There were no significant deviations when calculating the losses with the three cases (*Case 1*, *Case 2* and *Case 3*). The effect of B_r in the magnet losses was negligible. Lastly, the simulations with zero speed of the rotor yielded a reduction of the simulation time of 28%. Same conclusion would be drawn at 100 kHz.

V. Results Analysis and Comparison

Figure 14 summarizes the losses calculated with the selected analytical models and with 2D and 3D-FEM simulations. The calculations of losses in the magnet were performed at frequencies from 10 to 100 kHz. As the frequency increases, model *Huang_a* neglecting the skin effect, shows the highest deviation. In contrast, the model *Huang_b* shows a similar trend when compared with 2D-FEM results but still with a large deviation. Regarding model *Zhu*, the results show not only a similar trend but also the lowest deviation. This allows to confirm that model *Zhu* may be applied to a slotless machine with a diametrically magnetized ring. However, there is a large deviation between the results of 2D and 3D-FEM.

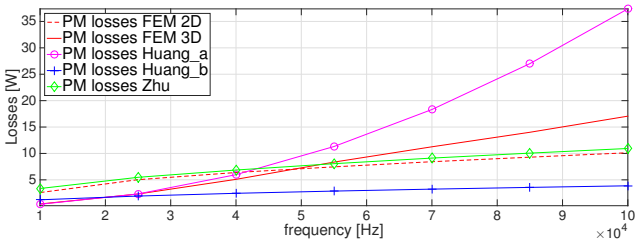

Fig. 14: Losses vs frequency 2D-FEM, 3D-FEM and analytical models.

Table II summarizes the values of losses obtained with both 2D and 3D-FEM calculations with their respective deviations at frequencies of 10, 40, 70 and 100 kHz for a magnet length of *l*. Values of the magnetic flux density in the air-gap $B_{\delta w}$ are also included.

TABLE II: Magnet losses vs. frequency 2D and 3D-FEM.

Freq. [kHz]	Loss magnet length=*l*			$B_{\delta w}$		
	2D FEM [W]	3D FEM [W]	ΔError [%]	2D FEM [mT]	3D FEM [mT]	ΔError [%]
10	2.59	0.44	-83.01	9.83	14.43	46.80
40	6.39	4.99	-21.91	6.51	13.11	101.38
70	8.43	11.16	32.38	5.35	11.99	124.11
100	10.13	16.96	67.42	4.75	10.01	110.74

At 100 kHz, the losses calculated with 3D-FEM are 67.42 % higher than predicted by 2D-FEM. In contrast, the simulation times were of 4419 and 660 seconds, respectively. The explanation to such large deviations at both low and high frequencies is the reaction field of eddy currents B_{eddy}. In 2D-FEM simulations, the end-effects are neglected, the equivalent impedance seen by the current is low and the eddy currents flowing in the magnet are high as a result. As a consequence, the reaction field of eddy currents B_{eddy} is higher and increasing with frequency. The magnetic flux density in the air-gap $B_{\delta w}$ is being reduced, which in return, yields lower losses. This is confirmed in table II where $B_{\delta w}$ for 2D-FEM has a diminution of its value of around 50 %. On the other hand, for 3D-FEM simulations, the eddy currents

described a different flow path, including the end-effects. The impedance seen by the current is much higher and consequently the eddy currents are more limited, resulting in a lower value. This is clarified in table II, where the value of $B_{\delta w}$ is reduced by approximately 30 %.

The investigation was extended to the case in which the magnet length l was affected by a factor of 2. The motivation for this selection, is to show that for a given value of l, the deviation between the losses calculated with both 2D and 3D-FEM should start reducing. The reduction of the deviation between 2D and 3D-FEM simulations is around 27% and 12% at lower and higher frequencies, respectively. In addition, the losses for a magnet length of l and $2l$ are shown in figure 15. The results from 2D-FEM simulations correspond to the values calculated in Subsection IV-A multiplied by 2. In figure 15, two frequencies at which the calculated losses in both 2D and 3D-FEM simulations are equal exist. These frequencies are at around 48 kHz for l and 30 kHz for $2l$. As the length of the magnet increases, the curve representing the losses calculated by 2D-FEM starts approaching to the curve representing 3D-FEM results as expected. This happens when the end-effect of the returning loop for the current in 3D-FEM simulations start to be insignificant (i.e., $l \gg w$).

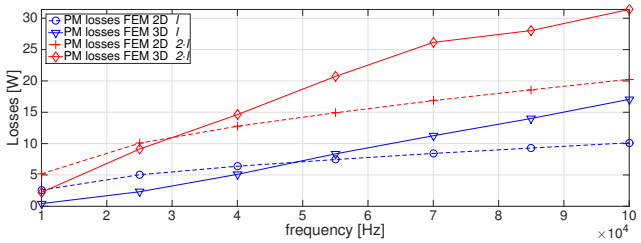

Fig. 15: Magnet losses comparison 2D and 3D-FEM simulations with l and $2l$.

VI. Conclusions

A thorough investigation of FEM simulation settings for calculating magnet losses in a 2-pole PM motor was presented. It was shown that skin and end-effect are not negligible, requiring 3D-FEM simulations. The validity of losses values obtained with models needs to be confirmed. This can only be done through experimental measurements in the actual machine, dealing with the issue of separating the losses in the machine. Additionally, while doing measurements, the machine is fed by harmonic voltage sources. This means that, in another study, the amplitudes of the current harmonics will need to be derived accounting for the variation of the machine impedance with frequency introduced by the eddy currents in the magnets.

References

[1] J. Millinger, "Eddy-current losses in permanent magnets of PM machines due to PWM harmonics," Tech. report - KTH Royal Institute of Technology, June 2015.

[2] K. Shirabe, M. Swamy, J. K. Kang, M. Hisatsune, Y. Wu, D. Kebort, and J. Honea, "Advantages of high frequency pwm in ac motor drive applications," in *Energy Conversion Congress and Exposition (ECCE), 2012 IEEE*, Sept 2012, pp. 2977–2984.

[3] K. Binnemans and P. T. Jones, "Rare earths and the balance problem," *Journal of Sustainable Metallurgy*, vol. 1, no. 1, pp. 29–38, 2015. [Online]. Available: http://dx.doi.org/10.1007/s40831-014-0005-1

[4] M. Markovic and Y. Perriard, "Analytical solution for rotor eddy-current losses in a slotless permanent-magnet motor: The case of current sheet excitation," *Magnetics, IEEE Transactions on*, vol. 44, no. 3, pp. 386–393, March 2008.

[5] A. Qazalbash, S. Sharkh, N. Irenji, R. Wills, and M. Abusara, "Rotor eddy current power loss in permanent magnet synchronous generators feeding uncontrolled rectifier loads," *Magnetics, IEEE Transactions on*, vol. 50, no. 6, pp. 1–9, June 2014.

[6] J. Klotzl, M. Pyc, and D. Gerling, "Permanent magnet loss reduction in pm-machines using analytical and fem calculation," in *Power Electronics Electrical Drives Automation and Motion (SPEEDAM), 2010 International Symposium on*, June 2010, pp. 98–100.

[7] M. Mirzaei, A. Binder, B. Funieru, and M. Susic, "Analytical calculations of induced eddy currents losses in the magnets of surface mounted pm machines with consideration of circumferential and axial segmentation effects," *Magnetics, IEEE Transactions on*, vol. 48, no. 12, pp. 4831–4841, Dec 2012.

[8] J. Wang, K. Atallah, R. Chin, W. Arshad, and H. Lendenmann, "Rotor eddy-current loss in permanent-magnet brushless ac machines," *Magnetics, IEEE Transactions on*, vol. 46, no. 7, pp. 2701–2707, July 2010.

[9] K. Yamazaki and Y. Fukushima, "Effect of eddy-current loss reduction by magnet segmentation in synchronous motors with concentrated windings," *Industry Applications, IEEE Transactions on*, vol. 47, no. 2, pp. 779–788, March 2011.

[10] M. K. Kazimierczuk, "Skin effect," in *High-Frequency Magnetic Components*, 2nd ed. Chichester, UK: John Wiley and Sons, 2013, ch. 3.

[11] C. Carstensen, "Eddy currents in windings of switched reluctance machines." Ph.D. dissertation, RWTH Aachen University, 2007.

[12] W.-Y. Huang, A. Bettayeb, R. Kaczmarek, and J.-C. Vannier, "Optimization of magnet segmentation for reduction of eddy-current losses in permanent magnet synchronous machine," *Energy Conversion, IEEE Transactions on*, vol. 25, no. 2, pp. 381–387, June 2010.

[13] J. R. Brauer, Z. Cendes, B. Beihoff, and K. P. Phillips, "Laminated steel eddy-current loss versus frequency computed using finite elements," *Industry Applications, IEEE Transactions on*, vol. 36, no. 4, pp. 1132–1137, Jul 2000.

[14] Z. Zhu, K. Ng, N. Schofield, and D. Howe, "Improved analytical modelling of rotor eddy current loss in brushless machines equipped with surface-mounted permanent magnets," *Electric Power Applications, IEE Proceedings* -, vol. 151, no. 6, pp. 641–650, Nov 2004.

[15] Z. Zhu and D. Howe, "Instantaneous magnetic field distribution in brushless permanent magnet dc motors. ii. armature-reaction field," *Magnetics, IEEE Transactions on*, vol. 29, no. 1, pp. 136–142, Jan 1993.

VII. Biographies

Adolfo Garcia Gonzalez received his M.Sc. degree in Electrical Engineering from KTH Royal Institute of Technology, Sweden, in 2015. He is currently working toward a Ph.D. degree at the Section of Electrical Machines of the Department of Energy Technology at Aalborg University. His research interests include modelling and design of electrical machines with 3D-Flux and non-traditional materials for traction applications.

Jonas Millinger received his M.Sc. degree in Electrical Engineering from KTH Royal Institute of Technology in 2011. Since 2010, he has been with Atlas Copco Industrial Technique (Stockholm) involved in the design of electrical machines for power tools. He is currently working toward an industrial Ph.D. degree at the Department of Electric Power and Energy Systems, KTH Royal Institute of Technology. His research interests include modelling and design of electrical machines, with a current focus on harmonic loss modelling and motor-drive system optimization.

Juliette Soulard (M'00) received the Ph.D. degree from the University of Paris VI, France, in 1998. She is Associate Professor with the Department of Electric Power and Energy Systems, leading the Electrical Machines and Drives laboratory at KTH Royal Institute of Technology, Stockholm, Sweden. Her research interests include modelling and design of electrical machines, with a current focus on losses and thermal modelling.